# In vivo co-registered hybrid-contrast imaging by successive photoacoustic tomography and magnetic resonance imaging

## Author Information

### Affiliations

**Guangdong Provincial Key Laboratory of Medical Image Processing and School of Biomedical Engineering, Southern Medical University, Guangzhou, Guangdong, China**

Shuangyang Zhang, Li Qi, Xipan Li, Zhichao Liang, Jian Wu, Shixian Huang, Jiaming Liu, Zhijian Zhuang, Yanqiu Feng, Qianjin Feng and Wufan Chen

### Contributions

L.Q. and S.Z. conceived the project idea and initiated the research. S.Z., S.H., Q.F and L.Q. conceived and designed the dual-modality animal imaging bed. S.Z, X.L. and L.Q. developed all software algorithms. S.Z., J.W. and J.L. carried out the animal experiments. S.Z. and Z.L. analysed the data. S.Z. realized the final images. L.Q., S.Z. and W.C. wrote the paper. All the authors discussed the results and revised the paper.

### Corresponding authors

Correspondence to: Li Qi and Wufan Chen

## Abstract

Magnetic resonance imaging (MRI) and photoacoustic tomography (PAT) are two advanced imaging modalities that offer two distinct image contrasts: MRI has a multi-parameter contrast mechanism that provides excellent anatomical soft tissue contrast, whereas PAT is capable of mapping tissue physiological metabolism and exogenous contrast agents with optical specificity. Attempts have been made to integrate these two modalities, but rigid and reliable registration of the images for in vivo imaging is still challenging. In this paper, we present a complete hardware-software solution for the

1

24  successive acquisition and co-registration of PAT and MRI images in *in vivo* animal studies. Based on

25  commercial PAT and MRI scanners, our solution includes a 3D-printed dual-modality animal imaging

26  bed, a 3-D spatial image co-registration algorithm with bi-model markers, and a robust modality

27  switching protocol for in vivo imaging studies. Using the proposed solution, we successfully

28  demonstrated co-registered hybrid-contrast PAT-MRI imaging that simultaneously display multi-scale

29  anatomical, functional and molecular characteristics on healthy and cancerous living mice. Week-long

30  longitudinal dual-modality imaging of tumor development reveals information on size, border, vascular

31  pattern, blood oxygenation, and molecular probe metabolism of the tumor micro-environment at the same

32  time. Additionally, by incorporating soft-tissue information in the co-registered MRI image, we further

33  show that PAT image quality could be enhanced by MRI-guided light fluence correction. The proposed

34  methodology holds the promise for a wide range of pre-clinical research applications that benefit from the

35  PAT-MRI dual-modality image contrast.

## Introduction

37  Tomographic imaging of living animals has been an important task for preclinical research because it

38  provides cross-sectional images of the subject without surgical intervention. This unique capability has

39  differed it from other transmissive or reflectance imaging approaches such as whole body fluorescence

40  imaging[1] or digital radiography[2]. Among many tomographic imaging techniques, Photoacoustic

41  Tomography (PAT) and Magnetic Resonance Imaging (MRI) are two advanced biomedical imaging

42  modalities that have been used in various pre-clinical imaging applications ranging from tumor

43  screening[3-7], therapy evaluation[8-10], to functional brain imaging[11-16] and so on. In PAT, an image that maps

44  the original energy deposition inside the target is formed by detecting and processing the ultrasonic

45  signals generated by laser illumination[17,18]. PAT is able to reveal the distribution of endogenous tissue

46  absorbers, such as oxyhemoglobin ($HbO_2$) and deoxyhemoglobin (Hb), and exogenous optical probes,

47  such as the FDA approached Indocyanine Green (ICG), by identifying their absorption spectrum under

48  multiple wavelength excitations[19-21]. On the other hand, as a Nobel winning technology, MRI provides

49    cross-sectional images of the subject by using non-ionizing electromagnetic radiation and measuring the

50    nuclear magnetic resonance signal, and thus enables multitudinous tissue contrast. MRI is able to provide

51    comprehensive, multi-parametric information on anatomy, function and metabolism. Thanks to the

52    emergence of diffusion MRI, functional MRI and other technologies, MRI has covered various clinical

53    neurological, psychiatric, cardiac and abdominal applications[22].

54       Given their outstanding imaging capabilities, these two imaging modalities are complementary at

55    multiple dimensions. Firstly, they have distinct image contrast mechanisms. PAT provides molecular

56    imaging capability that reflects the optical characteristics of light absorbers inside tissue[23-25], whereas

57    MRI images the density of hydrogen protons such that soft-tissue contrast is revealed. Secondly, the

58    imaging speeds are complementary. Thanks to recent advancement in laser technology, PAT imaging

59    speed could reach over 7000 frames per second[26], whereas high-field MRI system could only acquire at

60    most one to two images per second without scarifying image quality[27]. Thirdly, their spatial resolutions

61    are matched. Common spatial resolutions for commercial pre-clinical MRI and PAT scanners are both

62    around tens to hundreds micrometres[28] given an imaging field of view of several square centimetres.

63    Finally, PAT and MRI also share the advantages of being non-invasive, non-ionizing and label-free.

64       The benefits brought about by these complementary features of the two imaging technologies are

65    abundant and attractive. Due to the inherent low soft tissue contrast in PAT, it is difficult to precisely

66    identify the anatomical location of the targeted chromophores. With its combination with MRI, which

67    provides excellent anatomical definition and soft tissue contrast, this limitation might be removed and

68    accurate target lesion positioning and analysis could be achieved. Also, the high imaging speed of PAT

69    could compensate for its counterpart in MRI, making dynamic imaging of transient biological activities

70    such as neuron firing possible. Moreover, information sharing between the acquired dual-modality images

71    might be able to help improve the image quality of one another (e.g. the structural information provided

72    by MRI may be used to guide PAT image reconstruction or image recovery). PAT-MRI dual-modality

73    imaging that simultaneously acquires structural, functional, and molecular images has great potential to

74    push the image analyse focus to multiple scales, allowing for much broader preclinical research impacts.

75  Previous attempts to integrate images from these two modalities confined to either rigid registration

76  (e.g. imaging of rigid structures such as the brain[29,30]) or no registration[31-33]. Co-registration of abdomen

77  PAT and MRI images of small animals using a customized single-use silicone MRI holder has been

78  reported previously[34], which realized the registration of soft tissue images for the first time. Most recently,

79  a prove-of-concept concurrent PAT-MRI imaging system has been proposed with phantom-based

80  feasibility validation[35]. Development of such system requires high cost for customized instrumentation,

81  and sacrifices the flexibility of individual system. Apart from hardware registration, robust software

82  registration algorithms are required to precisely align the images from different modalities. Co-

83  registration of PAT and MRI images of the brain of small animals has been proposed[29]. It combines

84  mutual information based rigid registration algorithm with manually labelled anatomical landmark for the

85  matching of the brain, which is a non-deformed object.

86  Although there were these aforementioned early demonstrations of successive or concurrent PAT-MRI

87  imaging for various applications, implementing a rigidly co-registered, dual modality imaging solution

88  faced significant challenges. First, PAT imaging requires coupling media (e.g. water) whereas MRI

89  imaging does not. The purpose of the coupling media is to let the excited ultrasound to propagate.

90  However, during modality switching, this coupling media will inevitably affect the posture of the animal.

91  Second, MRI requires a strictly no-metal imaging environment, making the design and fabrication of a

92  robust bimodal registration tool difficult. Third, it requires spatial resolution matching at the axial, radial,

93  and tangential directions, simultaneously. Fourth, flexible, easy-to-use software compensation algorithms

94  for dual-modality image registration are required for high repeatability imaging experiments. Fifth,

95  similar to the attenuation correction in a Positron Emission Tomography/Computed Tomography

96  (PET/CT) scanner where CT image is used to enhance PET imaging, PAT-MRI requires mutual

97  connection and collaboration between the two modalities in order to excavate deeper information. Finally,

98  the obtained dual-model images from long-term in vivo longitudinal imaging should be validated, and the

99  performance of the whole imaging protocol should be benchmarked and analysed.

100     Here, we propose a method for the successive acquisition and co-registration of PAT and MRI data in

101     *in vivo* mice studies. The method includes a novel dual-modality imaging bed and a robust dual-modality

102     spatial co-registration protocol. The 3D-printed imaging bed is specifically designed to secure the posture

103     and position of the animals during modality switching. Based on this bimodal imaging bed, we design a

104     rigorous data acquisition procedure, a stable modality switching protocol, and a highly automated data

105     post-processing software suite to enable precise matching of the dual-modality images of the entire

106     animal body. We demonstrate the excellent capability of this successive PAT-MRI dual-modality imaging

107     method in *in vivo* applications including tomographic hybrid contrast observation of important organs

108     (simultaneously structural, functional, and molecular imaging), multi-timescale longitudinal monitoring

109     of tumor development (from minute-scale drug uptake to week-long evolution of tumor size and hypoxia

110     condition), and structural MRI guided light fluence correction for quantitative PAT. This integrated and

111     standardized protocol for in vivo small animal PAT-MRI dual-modality imaging will help unlocking and

112     promoting even more preclinical research applications of these two modalities, such as simultaneous

113     functional-anatomical brain imaging, bimodal contrast agent development, and anatomically specific

114     pharmacokinetic research and etc.

## Results

### Spatially co-registered successive PAT-MRI imaging.

117     We first describe the proposed co-registered successive PAT-MRI imaging solution. Our solution is

118     developed particularly for a 7-tesla MRI scanner (Pharmascan, Burker, Germany) and a commercial

119     multispectral cross-sectional PAT system (MSOT inVision128, iThera Medical, Germany), both of which

120     are among the most popular commercial imaging platforms for pre-clinical small animal imaging. The

121     radial resolution of the MRI and PAT systems were similar (~ 150 um). The axial resolution of MRI

122     could reached <100 um, but for the PAT it is limited to 800 um (see METHODS for detail). However, the

123     axial resolution of MRI is tunable such that the spatial resolutions, both axial and radial, are matched for

124     the two modalities. To ensure precise spatial co-registration of the animal during modality switching, our

125  solution includes a specially designed dual-modality imaging bed (Fig. 1 a). This bed consists of a gas

126  tube, a breathing mask, two fixing plates, two ancillary supports and a solid animal support that can be

127  separated into two parts, one for PAT, and the other for MRI. All the components except for the gas tube

128  are 3D printed with polylactic acid (PLA). The gas tube, made of rubber, was connected to the anesthesia

129  gas inlet and the breathing mask to keep the animal under anesthesia. In addition, a silicone sealing pad

130  was used to isolate the frontal part of the mouse head from water during PAT imaging. During the MRI

131  imaging, the MRI support could be fitted into the original MRI animal bed. During the T2 spin echo

132  sequence, the PLA material of the support will not generate interference signal to the object. During PAT

133  imaging, the PAT support was firmly fixed on the original animal holder of the PAT system such that the

134  animal was placed right in the centre of the detector array.

135     The image acquisition process was divided into four steps (Fig. 1c, d, Supplementary Figure 1). 1)

136  Axial marker assignment: Chinese ink was used as markers for axial registration because it can be

137  visualized in both MRI and PAT. The ink was marked on the skin surface of nude mice using a Gauge 20

138  needle. The marker size was less than 1 mm and the separation distance was 1 cm such that minimum

139  interference is caused to the images. 2) MRI imaging: the animal was fastened on the MRI support and

140  transferred to the MRI imaging cavity, and the location of the mouse to be scanned was positioned in the

141  center of the RF coil. During MRI imaging, we used a 2-D spin-echo sequence to scan the axial image in

142  the XY plane. After the acquisition was completed, the dataset was resliced along the XZ and YZ

143  directions to obtain the coronal and sagittal images. 3) Support switching: First, we used screws to fasten

144  the MRI support on the fixing plates. Then, we unscrewed the screws on the cantilever and removed the

145  PAT support. During this process, the body of the mouse was always in a tight state that ensured an

146  unchanged posture. After the animal support was switched, exogenous contrast agent for PAT imaging

147  such as ICG could be injected. 4) PAT imaging: we fix the PAT support on the original animal holder of

148  the PAT system, and connect the gas tube to the anaesthesia port on the holder. The whole assembly was

149  then transferred to the imaging chamber filled with distilled water pre-heated to 34-degree Celsius. The

150  assembly was set on a built-in motorized translation stage, such that the animal could be positioned to the

151 optimal field of view. Finally, multi-spectral 3-D PAT image acquisition was carried out. When the PAT

152 imaging section was finished, the PAT support was taken out from the imaging chamber and the animal

153 was released. A video showing the above processes are available in Supplementary Video 1.

154 After the dual-modality imaging, post-processing of the acquired images were employed to refine the

155 co-registration. The post-processing procedures (Fig. 1e, Supplementary Figure 3) are as follows: 1) PAT

156 image reconstruction: to get rid of the effect of the PAT image background signal on the registration

157 result, we used a non-negative model-based iterative image reconstruction algorithm which limits the

158 signal value to positive during each iteration. 2) Axial registration: the ink markers on the skin surface of

159 nude mice can be visualized on both PAT and MRI, therefore, the corresponding axial position of the

160 images is found by locating the markers (see Supplementary Methods for details). 3) Transverse

161 registration: after the images were axially registered, we performed transverse registration on

162 corresponding PAT-MRI image slices by using a rigid co-registration algorithm based on mutual

163 information. This will compensate for the small shifting or rotation of the animal during modality

164 switching, and further align the dual-modality images. 4) Spectral un-mixing: for PAT images acquired

165 with multispectral excitation, we perform spectral un-mixing to identify the distribution of endogenous

166 ($HbO_2$, Hb) or exogenous absorbers (such as ICG) from the background. The un-mixing is based on a

167 linear algorithm[21] with multispectral PAT images as inputs. 5) Light fluence correction: to account for the

168 light attenuation during its propagation in tissue, we make use of the rich and clear soft-tissue contrast in

169 MRI to guide the estimation of the light fluence distribution during PAT imaging, and design an iterative

170 algorithm (see METHODS for detials) to correct for the light attenuation. The obtained corrected PAT

171 images not only show evenly distributed image intensity, but also represent quantitative optical

172 absorption and scattering coefficients of different tissues.

173 ## Co-registered anatomical imaging by PAT and MRI.

174 With the proposed successive PAT-MRI dual-modality imaging method, we achieved three-dimensional

175 co-registered anatomical imaging of healthy and tumorous mice *in vivo*. Supplementary Fig. 4a shows the

176   corresponding PAT and MRI images at the ink marker position. In the MRI image, the ink marker can be

177   localized easily, however, in the PAT image, the marker spreads for nearly 5 mm along the axial direction

178   (Supplementary Fig. 4b) due to its strong optical absorption, making the identification of the correct PAT

179   slice difficult. To tackle this, we quantified the intensity of the marker at each slice, as plotted in

180   Supplementary Fig. 4c, and then applied Gaussian fitting to the plot. The PAT image at the peak position

181   of the fitted curve was considered to be the correct image that matched the MRI image. Fig. 2a, b show

182   the co-registration results of the healthy and tumorous nude mouse respectively. By resampling and

183   interpolating the XY plane image stack, we obtained the sagittal and coronal images and displayed them

184   in 3D as volume images. The joint visualization of the PAT and MRI images reveals successful matching

185   of the internal structure and the consistency of the body shapes of the animal. The kidneys, spleen and

186   spine in the axial image of healthy nude mice are correctly overlapped, and the body contours are also

187   consistent. The tumorous mice datasets furthered demonstrated the robust performance of the co-

188   registration strategy across week-long continuous dual-modality screening. The bright area around the

189   centre of the tumor in the PAT image, which indicated a decrease of blood oxygen saturation, accurately

190   matched that of the MRI image that showed weaken T2 signal (Supplementary Fig. 5). Finally, we

191   perform quantitative evaluation of the registration performance (Fig. 2c) using the Dice Similarity

192   Coefficient (DSC), which measures the percentage of the overlap between the two images (See

193   Supplementary Methods). The average DSCs for healthy and tumorous mice are 93.06% and 95.12%

194   respectively, demonstrating very high overlap between the PAT and MRI images.

## Hybrid-contrast longitudinal recording of tumor growth.

196   To demonstrate the capability of simultaneously anatomical and functional imaging, PAT-MRI dual-

197   modality longitudinal observation on nude mice bearing 4T1 tumor was performed. The successive

198   imaging was carried out on day 3, 5, 7, 9, 11, 13 and 17 post tumor implantation. MRI-T2 images that

199   represent structural information and $HbO_2$, Hb, HbT images that show hypoxia microenvironment

200   obtained from spectrally un-mixed multispectral PAT images. The image registration results and the

8

201　distribution of $HbO_2$ and Hb separated from the multispectral PAT images are shown in Supplementary

202　Fig. 6. To facilitate better visualization, we used the registered MRI images as a structural priori to

203　manually segment the tumor. As shown in the dual-modality images taken at day 17 (Fig. 3a), the MRI-

204　T2 image showed highly corresponding tumor geometry that matched the distribution of Hb, $HbO_2$, and

205　HbT. The white solid-line area depicts the regions with consistent or diametrically opposite features on

206　these images (darker in the T2 and brighter in the Hb and HbT). T2 signal represents changes in blood

207　oxygenation, and weakens when the concentration of Hb inside the tumor increases. To further analysis

208　the correlation between the obtained structural and functional information, profiles (Fig. 3b) of the Hb,

209　$HbO_2$, and HbT images were obtained along the white dashed-lines (Fig. 3a) and then compared with that

210　of the MRI image to calculate the Pearson Correlation Coefficient (PCC) (Fig. 3c). The PCC values

211　between T2 and Hb, $HbO_2$ and HbT are -0.9069, -0.0048 and -0.9062, respectively. The profiles show

212　opposite spatial trends between T2 and Hb, HbT across the tumor, and the PCC values close to -1 further

213　illustrate the negative correlation of this spatial variation. Overall, the inspection of T2 and Hb revealed

214　the existence of negative correlation, which became higher with time (Supplementary Fig. 6). Moreover,

215　as shown in a series of 3D fusion display using T2, Hb and $HbO_2$ images obtained during the tumor

216　development in Fig. 3d, the growth of the tumor was accompanied by the development of neovasculature

217　and the increase of tumor dimension. We also measured the change of tumor volume (Fig. 3e) from the

218　MRI images and calculated the values of tumor oxygen saturation (Fig. 3f) from the distribution of Hb

219　and $HbO_2$. Quantitative parameters obtained from the PAT images indicated that during tumor growth,

220　the Oxygen Saturation ($SO_2$) increased continuously from 60.67 % on day 3 to 72.96 % on day 7 for the

221　whole tumor area and decreased from 40.68 % on day 9 to 17.08 % on day 17 for the tumor center alone.

222　The overall volume of the tumor reached a 6-fold increase from 47.73 $mm^3$ on day 3 to 339.75 $mm^3$ on

223　day 17. In addition, the volume of the central region of the tumor saw a 40-fold increase from 0.44 $mm^3$

224　on day 7 to 17.7 $mm^3$ on day 17. This experiment demonstrated the unique capability of label free, long

225　term structural and functional hybrid contrast imaging of the PAT-MRI bimodal imaging method.

## 226 Spatially localized high-speed imaging of molecular probes.

227 To harness the high speed imaging capability provided by PAT imaging, we applied intravenous (IV)

228 injection of 200 μl of ICG (0.05 μg/μl) on a day-21 4T1 tumorous mouse after MRI imaging, and then

229 performed PAT temporal imaging of the mouse at 5-minute intervals for 40 mins. ICG, which is a FDA-

230 approved NIR fluorochrome commonly used as a contrast agent in retinal and tumor imaging, is able to

231 metabolize in blood-rich organs and excreted into the bile within one hour[36-38]. The registration results

232 and the distribution of ICG identified from the multispectral PAT images are shown in Supplementary Fig.

233 7. Fig. 4a shows the volumetric images of MRI-T2, $HbO_2$, Hb and ICG at various time points. As can be

234 seen, almost immediately after the injection, a small amount of ICG signal appeared in the tumor. Then

235 the signal gradually increased, indicating fast deposition of the ICG inside the tumor. Nevertheless, ICG

236 only appeared in the boundary region of the tumor, and its concentration in the central region was

237 relatively low across the whole imaging period. This indicated a hypoxic area had been developed in the

238 center of the tumor. Furthermore, we measured the ICG concentration at different time at both the centre

239 and boundary regions of the tumor, and the result was shown in Fig. 4b. As can be seen, after ICG

240 injection, there was no significant change in its concentration around tumor centre (< 5 % fluctuation).

241 However, the ICG concentration in the boundary kept on rising around the first 20 minutes and reached a

242 peak increase of 39.12 % at t = 20 minute, and then slowly went down. This preliminary demonstration of

243 spatially localized continuous monitoring of contrast agent reveals the potential of our proposed method

244 for structural enhanced dynamic molecular imaging.

## 245 MRI assisted light fluence correction for quantitative PAT.

246 PAT image is the product of the absorption coefficient and the light fluence distribution[39,40]. Because light

247 attenuates as it propagates into deeper tissue, to determine the concentration of the chromophores, this

248 light attenuation effect has to be corrected. To eliminate the light fluence from the PAT image and

249 recover the distribution of the optical absorption coefficient is of great significance. Light fluence

250 correction method thatrequired the segmentation of the image at organ level are proposed previously to

251    estimate the optical parameters of each region[40]. However, it is difficult to perform accurate organ

252    segmentation on the PAT images alone because of its poor tissue contrast. Incorporation of co-registered

253    MRI images might be able to solve this problem. Here, we propose MRI structural information guided

254    light flucence estimation and correction for PAT. This method performs segmentation on the registered

255    MRI image acquired with our dual-modality imaging approach, and then uses the segmentation result to

256    guide the estimation of light fluence distribution (see METHODS and Supplementary Fig. 8).

257       We first performed validation of the method on phantom imaging experiments, and the results are

258    shown in Supplementary Fig. 9. The phantom is a cylindrical tissue mimicking phantom with three rod-

259    shape inclusions, which contained the same material at the same concentration. As can be seen, because

260    of light attenuation, the signal intensity of the inner rod is lower than the outer rods in the uncorrected

261    PAT image. In the corrected image, this attenuation effect has been successfully compensated for using

262    the proposed algorithm. The profiles (Supplementary Fig. 9b) drawn along the three rod shape inclusions

263    show that their photoacoustic signal intensity has returned to the same level after correction.

264       Next, we applied the proposed light fluence correction algorithm to the *in vivo* healthy nude mice data.

265    Fig. 5a shows the light fluence correction results at the neck and the kidney position, including the raw

266    PAT image (PAT), the registered MRI image (rMRI), the regions segmented on the MRI image (Prior),

267    the light fluence distribution obtained from the optimization algorithm (Fluence), and the corrected PAT

268    image (cPAT). As expected, the light fluence decreases radially from the surface to the center of the

269    animal body. With the application of light fluence correction, the signal around the image centre has been

270    significantly enhanced. And the inner kidney and the outer kidney have achieved similar signal strength

271    compared with the original PAT image. Fig. 5b shows the 3D light fluence distribution obtained by using

272    the proposed MRI-guided light fluence simulation method. As shown in Fig. 5c, after correction, the

273    visibility of the blood vessels deep inside the body have also be enhanced. The proposed dual-modality

274    PAT-MRI imaging strategy made it possible to incorporate the MRI structural information into the light

275    fluence correction process of PAT imaging, and the above experiments have successfully demonstrated

276    the feasibility of this technique.

## Discussion

278   Visualization of complementary information derived from different imaging methods provides multiple

279   types of image contrast, such that hidden information of the research problem may be revealed. Imaging

280   performed successively on different modalities saves the flexibility of individual modality, but the imaged

281   animal is easily deformed during modality switching, resulting in anatomy dislocation of the acquired

282   images. This problem makes it difficult to accurately share information provided by the imaging methods

283   because the image contrasts are misaligned. For successive PAT-MRI imaging, on one hand, the

284   structural and functional contrasts, spatial resolutions, and imaging speeds of the two methods are

285   perfectly complementary, making the implementation of such dual-modality imaging attractive. On the

286   other hand, however, since the animal fixation methods for the two modalities are very different, the

287   aforementioned registration problem becomes much more challenging.

288      The presented work provides a unique strategy for meeting this challenge. To ensure the posture and

289   position of the animal during modality switching, our successive PAT-MRI imaging method involves a

290   hardware registration device and a software toolset with automatic processing capability. On the hardware

291   side, a novel small animal dual-modality imaging bed was designed. This 3D-printed imaging bed solves

292   the water coupling problem in PAT imaging and ensures that the animal does not deform or displace

293   while switching between MRI and PAT. Its introduction preserves the consistency in the shape of the

294   entire mouse body or local lesion contour such as tumor boundary, and thereby simplifies the multi-

295   modality image co-registration problem into a rigid registration problem solvable by standard image

296   processing algorithms. Moreover, animal fastening method of the designed imaging bed was similar to

297   that of the original PAT system. Therefore, PAT imaging artefacts induced by the bed was minimized and

298   animal preparation time was not increased. The use of the breathing mask allowed for the animal to

299   breathe freely underwater during PAT imaging and ensured high survival rate of the animals. Also,

300   assembling and disassembling procedures of the MRI/PAT supports were designed to be both

301   convenience and stable, such that changes in animal pose and position were subtle. The animal bed is

302   simple to manufacture, low cost, reusable, and compatible with the harsh MRI environment. On the

303    software side, an axial registration method based on external dual-modality markers and a transverse co-

304    registration algorithm based on mutual information between MRI and PAT were developed to further

305    improve image co-registration performance. The Chinese ink marked on the animal surface is not only

306    minimum invasive and harmless, but also has PAT-MRI dual contrast. With the above unique advantages,

307    our proposed dual-modality imaging strategy offers a unified, standardized, and convenient solution to

308    implement successive acquisition of PAT and MRI images for *in vivo* preclinical animal research.

309        Furthermore, the feasibility of the proposed strategy was demonstrated in various dual-modality

310    imaging scenarios. Firstly, healthy nude mouse and cancerous nude mouse spatial co-registration results

311    showed high overlap of animal anatomy on the two images, illustrating the robustness and favourable

312    performance of the proposed strategy. Secondly, dual-modality characterization of spatial and temporal

313    heterogeneities of the hypoxia tumor microenvironment visualized vascular pattern changes throughout

314    the entire tumor development period, revealing the possibility of label-free, multi-contrast monitoring of

315    cancer development. Thirdly, high speed spatial and temporal tomographic imaging of exogenous contrast

316    agent uptake inside tumor demonstrated highly accurate structural localization of the imaging probe,

317    allowing for the study of drug metabolism dynamics with high spatial specificity. Finally, we found that

318    simple manual segmentation on MRI-T2 images provides valuable structural guidance to enhance the

319    estimation of light fluence distribution in PAT imaging. This enabled accurate light fluence correction of

320    the PAT images, and resulted in improvement of the visualization of deeply suited organs and

321    vasculatures.

322        Based on our work, we envision vast applications by the proposed successive PAT-MRI imaging

323    technology. For example, some studies have shown that the central hypoxia of solid tumors is related to

324    prognosis and treatment resistance[41,42]. Therefore, longitudinal quantitative analysis of $SO_2$ and HbT with

325    PAT imaging, which is able to access the hypoxic micro-environmental changes, and longitudinal tumor

326    morphology observation with MRI imaging, which can monitoring tumor dimension and growth rate, can

327    work together to provide a platform for the *in vivo* and *ex vivo* evaluation of anticancer therapies aimed at

328    reducing hypoxia and inhibiting tumor angiogenesis[42,43].

329    In this work, we have demonstrated the feasibility of an image acquisition and co-registration method

330    for PAT and MRI. The design of the dual-modality animal imaging bed ensures that the deformation of

331    the animal is within acceptable range when switching imaging modalities, thereby simplifying image co-

332    registration. The dual-modality hybrid-contrast image obtained with our method simultaneously provides

333    functional and structural information. This simple and reliable method can be widely implemented for

334    various PAT-MRI dual-modality *in vivo* animal studies.

## Methods

335

### PAT-MRI dual-modality imaging bed.

336

337    The major purpose of the dual-modality animal imaging bed is to ensure that the animal maintains at the

338    same positioning and posture during successive PAT and MRI imaging. Because the animal has to be

339    bathed in water during PAT imaging, the biggest challenge is to make sure the animal position does not

340    changed during the switching between the two imaging modalities. This was achieved by designing the

341    animal bed according to the PAT and MRI system environment and geometric dimensions. The dual-

342    modality imaging bed can be separated into two parts, one for PAT, and the other for MRI. All the

343    components except the gas tube were 3D-printed with PLA material using a desktop 3D printer (Jenny3D,

344    China).

345    *Gas tube*. A 10 mm diameter tube that connects the anaesthetic port to the breathing mask. The gas tube is

346    made of rubber and therefore it can supply the anaesthetic gas to the animal while preventing water from

347    entering the mask.

348    *Breathing mask*. The breathing mask functions like a swimming goggle except that it only covers the

349    mouth and nose of the animal. It includes a funnel-shaped structure, a built-in copper wire, and a sealing

350    silicone pad. One small end of the mask is connected to the anaesthetic port through the gas tube. The

351    other end of the mask is sealed with a silicone pad with a small hole in the center, such that the frontal

352    part of the mouth head fits into the hole. The copper wire is mounted transversely inside the breathing

14

353    mask for hooking the teeth of the mouse during PAT imaging. In this way, the mouse face can be closely

354    fitted to the silicone sealing pad, and drowning of the animal can be prevented. The mask also helps to

355    keep the mouse head steady during imaging.

356    *Fixing plates and ancillary supports*. Both the left and right sides of the imaging bed contained the fixing

357    plate and the ancillary support. The functions of the two fixing plates include: 1) to fix the animal onto the

358    PAT and MRI supports, and 2) to bind the limbs of the mouse and fix the breathing mask. These fixing

359    plates can be firmly attached to the imaging supports by using plastic or copper screws, and then the arms

360    and legs of the animal can also be tied to the support. The two ancillary supports are used to support the

361    torso of the mouse. The interested imaging regions can be selected by simply adjusting the positions of

362    the two ancillary supports. Supplementary Fig. 2 demonstrates four types of fixing plates and ancillary

363    supports for the imaging of different parts of the animal body.

364    *PAT support*. It includes two components: the mounting plate and the cantilever, which were assembled

365    by screw combination. The mounting plate can be perfectly attached on the original animal holder of the

366    PAT system, and can be translated in the axial direction of the nude mouse (less than 1cm) to facilitate the

367    connection of the gas tube. The cantilever was fastened to the fixing plates by screws such that the animal

368    to be imaged is in a suspended state. This design centers the animal in the ring-shape detector, and lets

369    none obstruction appeared along the sound propagation path. In this way, the PAT image quality can be

370    ensured.

371    *MRI support*. A curved base-plate used to fix the animal during MRI imaging by screwing to the fixing

372    plates. The MRI support is adapted to the body contour of the animal, prevents the animal from

373    deformation, and matches the shape of the original MRI bed.

374    ## Spatial co-registration algorithm of the PAT and MRI images.

375    The spatial co-registration algorithm of the PAT and MRI images contains the following steps. Step 1)

376    image pre-processing: perform image reconstruction, denoising, and background removal on the collected

15

377  multi-modal data. Step 2) axial registration with external markers: locate the corresponding position of

378  the multi-modality cross-sectional images by Gaussian fitting. Step 3) 2D transverse co-registration:

379  register the 2D bi-modal images with an automated rigid transverse registration algorithm. Evaluation of

380  co-registration accuracy by calculating the DSC was performed after the above software co-registration

381  was done. The schematic of the proposed spatial co-registration algorithm is shown in Supplementary Fig.

382  3.

## Light fluence estimation and correction method.

384  The PAT images are formed by reconstructing the original point source of the ultrasonic waves generated

385  by absorbing the laser pulse, and the pixel value $p(\vec{r})$ in the image is expressed as:

$$p(\vec{r}) = \alpha \Gamma u_a(\vec{r}) \Phi \left[ (\vec{r}), u_a(\vec{r}), u_s^{'}(\vec{r}) \right], \tag{1}$$

387  where $\alpha$ denotes the system response, $\Gamma$ denotes the thermo-elastic Gruneisen parameter, $u_a(\vec{r})$ and

388  $u_s^{'}(\vec{r})$ denotes the absorption coefficient and the scattering coefficient, $\Phi$ denotes the light fluence

389  within a voxel at the position $\vec{r}$. To perform light fluence correction, we first simulate the light fluence

390  distribution $\Phi$ over the imaging field-of-view, and then calculate the fluence corrected PAT image by $\Phi$

391  using the following equation:

$$u_a(\vec{r}) = \frac{p^{'}(\vec{r})}{\Phi \left[ (\vec{r}), u_a(\vec{r}), u_s^{'}(\vec{r}) \right]}, \tag{2}$$

393  where we make the reasonable assumption that $p^{'}(\vec{r})$ has been reconstructed from the acoustic

394  measurements accurately and with negligible structural distortion[17,18].

395  To make use of the structural information provided by the MRI images, we designed and implemented an

396  iterative optimization method to calculate the absorption and scattering coefficients. The schematic of the

397  algorithm is as shown in Supplementary Fig. 8. To improve the convergence speed of the absorption

16

398    coefficient $u_a$ optimization, we manually segmented the registered MRI images into different organ

399    regions $R_N$. These regions exhibited small changes in hemoglobin content and oxygen saturation, and

400    therefore the optical parameters could be considered uniform within an individual region. The

401    segmentation result was later used as prior information for light fluence estimation. We assigned

402    specifically one absorption coefficient and one scattering coefficient to each region according to

403    reference[40,44] and then use this as a constraint to solve the light fluence simulation problem. In the

404    optimization algorithm, the light fluence distribution was modelled by the diffusion equation, and solved

405    by using the Toast++ toolbox[45] in MATLAB (Mathworks, US). The finite element method (FEM) was

406    employed in the Toast++ toolbox to model the light transport inside the object and the optimization of the

407    objective function was implemented with the built-in minimization function 'fmincon' in MATLAB. For

408    initialization, the absorption coefficient varied from 0 mm$^{-1}$ to 1 mm$^{-1}$, and the scattering coefficient was

409    limited to be within a $\pm$ 10% variation range.

## Animal models.

411    All animal experiments were approved by the local Animal Ethics Committee of Southern Medical

412    University and were performed in accordance with current guidelines. In the *in vivo* animal imaging

413    experiment, 6 healthy nude mice (12-15 g/each, female, Southern Medical University, Guangzhou, China),

414    and 4 nude mice carrying 4T1 mammary carcinoma (Southern Medical University Cancer Institute,

415    Guangzhou, China) were used. Animals were kept in ventilated cages inside a temperature-controlled

416    room, under a 12-h dark/light cycle. In order to reduce abdominal peristalsis artifacts caused by food

417    digestion and to prevent the mice from excreting and polluting the imaging environment during PAT

418    imaging, the nude mice were fasted for 8 hours before imaging.

## Magnetic resonance imaging.

420    All MRI scan were performed on a 7 T small animal MRI system (Pharmascan, Bruker, Germany)

421    operated by ParaVision 6.0 software platform. A 1H transmit-receive volume coil with 40 mm inner

17

422   diameter was used for signal transmitting and receiving. The animal was anesthetized with 4 % chloral

423   hydrate at 0.01 ml/g. We assembled the MRI support, fixed the limbs of the anesthetized animal on the

424   fixing plates on both sides, and hooked the teeth of the nude mouse on the copper wire in the breathing

425   mask. In order to reduce the image artefacts caused by respiratory movements, medical oxygen mixed

426   with high concentration isoflurane (1%, RWD, China) was transmitted through the gas tube to the

427   breathing mask, so that the respiratory rate of nude mice was maintained at 15-20 times/min. The body

428   temperature of the nude mouse was monitored using the rectal probe of a small animal monitoring system

429   (Model 1030, Small Animal Instruments Inc., New York, NY, USA), and stabilized at $37 \pm 0.1$ °C using

430   the heater module. The T2 MRI images of nude mouse were obtained using a 2-D spin echo sequence

431   (Turbo rapid acquisition with refocused echoes) with the following imaging parameters: RARE factor 8,

432   echo time 10 ms, repetition time 6000 ms, 5 averages, slice thickness/gap 0.8/0.2 mm, field of view 25 ×

433   25 mm$^2$, matrix 250 × 250, spatial resolution $0.1 \times 0.1 \times 0.8$ mm$^3$. Sagittal T2 images of the YZ plane

434   where the markers located were firstly acquired. Based on these images, the slice direction and position of

435   the axial image was selected so that each marker was at the centre of the slice and the slice direction was

436   perpendicular to the long-axis of the animal. The axial T2 images covering either the upper or lower parts

437   of nude mouse were then acquired because the coil's effective imaging range was insufficient to cover the

438   entire mouse.

439   Photoacoustic tomography imaging.

440   A commercial small animal multispectral photoacoustic tomography system (MSOT inVision128, iThera

441   Medical, Germany, Fig. 1d) was employed to perform all the PAT imaging. A pulsed OPO laser (670 nm

442   - 960 nm tunable) with pulse width <10 ns, repetition rate of 10 Hz and a peak pulse energy of 60 mJ at

443   760 nm is employed in this PAT system. The laser light excites the sample through a ten-arm fiber bundle,

444   which provides a diffused, homogeneous, and 360-degree illumination over the surface of the animal. The

445   generated ultrasonic waves are detected by 128 toroidally focused ultrasound transducers with a centre

18

446 frequency of 5 MHz (60% bandwidth) arranged over an azimuth span of 270-degrees around the cylinder

447 with a radius of curvature of 41 mm (Fig. 1d).

448     When switching to PAT imaging, we needed to assemble the PAT support on the fixing plates with

449 screws first, and then removed the MRI support. This is to ensure that the posture of the animal did not

450 changed during the modality switching process. Finally, the animal-fixed PAT support was attached to

451 the original PAT holder which aligned it with the center of the transducer and immersed the animal in

452 34 ℃ heated water for ultrasonic coupling and warm keeping. All nude mice were anesthetized with 1%

453 isoflurane during imaging. Whole body imaging was realized by translating the PAT support axially with

454 the built-in motorized translation stage. For contrast enhanced PAT, an insulin injection needle was

455 embedded into the tail vein in advance, and was connected to a long Polyethylene Tubing 10 (PE 10) that

456 enabled contrast agents injection (such as ICG) from outside the imaging chamber. Multispectral PAT

457 images were acquired at five different illumination wavelengths: 700, 730, 760, 800 and 850 nm and

458 averaged with signals from 10 frames per wavelength. The ultrasound time series signals are then

459 reconstructed into 2D pressure maps using a model-based iterative reconstruction algorithm with a 30 ×

460 30 mm field-of-view at 300× 300 pixels. During image reconstruction, the pressure value is limited to

461 positive because the negative value only reflects the artifacts caused by the incomplete geometry of the

462 system. Finally, the linear unmixing algorithm[21] was used to calculate the distribution of $HbO_2$, Hb and

463 ICG.

464 ## Statistical analysis.

465 Matlab (MathWorks Inc.) and GraphPad Prism software (GraphPad Software Inc.) were used for

466 statistical analyses and graph drawing.

467 ## **Data Availability**

468 The data that support the findings of this study are available from the corresponding authors upon

469 reasonable request.

# References

1    Frangioni, J. V. In vivo near-infrared fluorescence imaging. *Current Opinion in Chemical Biology* **7**, 626-634, doi:https://doi.org/10.1016/j.cbpa.2003.08.007 (2003).

2    Chotas, H. G., Dobbins, J. T., 3rd & Ravin, C. E. Principles of digital radiography with large-area, electronically readable detectors: a review of the basics. *Radiology* **210**, 595-599, doi:10.1148/radiology.210.3.r99mr15595 (1999).

3    Ivankovic, I., Mercep, E., Schmedt, C. G., Dean-Ben, X. L. & Razansky, D. Real-time Volumetric Assessment of the Human Carotid Artery: Handheld Multispectral Optoacoustic Tomography. *Radiology*, 181325, doi:10.1148/radiol.2019181325 (2019).

4    Lin, L. *et al.* Single-breath-hold photoacoustic computed tomography of the breast. *Nat Commun* **9**, 2352, doi:10.1038/s41467-018-04576-z (2018).

5    Knieling, F. *et al.* Multispectral Optoacoustic Tomography for Assessment of Crohn's Disease Activity. *N Engl J Med* **376**, 1292-1294, doi:10.1056/NEJMc1612455 (2017).

6    Stoffels, I. *et al.* Metastatic status of sentinel lymph nodes in melanoma determined noninvasively with multispectral optoacoustic imaging. *Sci Transl Med* **7**, 317ra199, doi:10.1126/scitranslmed.aad1278 (2015).

7    Neuschler, E. I. *et al.* A Pivotal Study of Optoacoustic Imaging to Diagnose Benign and Malignant Breast Masses: A New Evaluation Tool for Radiologists. *Radiology* **287**, 398-412, doi:10.1148/radiol.2017172228 (2018).

8    Haedicke, K. *et al.* High-resolution optoacoustic imaging of tissue responses to vascular-targeted therapies. *Nat Biomed Eng* **4**, 286-297, doi:10.1038/s41551-020-0527-8 (2020).

9    Li, X. *et al.* Supramolecular Phthalocyanine Assemblies for Improved Photoacoustic Imaging and Photothermal Therapy. *Angew Chem Int Ed Engl* **59**, 8630-8634, doi:10.1002/anie.201916147 (2020).

10   Padhani, A. R. Functional MRI for anticancer therapy assessment. *Eur J Cancer* **38**, 2116-2127, doi:10.1016/s0959-8049(02)00388-x (2002).

11   Moonen, C. T., van Zijl, P. C., Frank, J. A., Le Bihan, D. & Becker, E. D. Functional magnetic resonance imaging in medicine and physiology. *Science* **250**, 53-61, doi:10.1126/science.2218514 (1990).

12   deCharms, R. C. Applications of real-time fMRI. *Nat Rev Neurosci* **9**, 720-729, doi:10.1038/nrn2414 (2008).

13   Logothetis, N. K. What we can do and what we cannot do with fMRI. *Nature* **453**, 869-878, doi:10.1038/nature06976 (2008).

14   Nasiriavanaki, M. *et al.* High-resolution photoacoustic tomography of resting-state functional connectivity in the mouse brain. *Proc Natl Acad Sci U S A* **111**, 21-26, doi:10.1073/pnas.1311868111 (2014).

15   Lv, J. *et al.* In vivo photoacoustic imaging dynamically monitors the structural and functional changes of ischemic stroke at a very early stage. *Theranostics* **10**, 816-828, doi:10.7150/thno.38554 (2020).

16   Wang, X. *et al.* Noninvasive laser-induced photoacoustic tomography for structural and functional in vivo imaging of the brain. *Nat Biotechnol* **21**, 803-806, doi:10.1038/nbt839 (2003).

17   Li, X. *et al.* Model-Based Optoacoustic Tomography Image Reconstruction With Non-local and Sparsity Regularizations. *Ieee Access* **7**, 102136-102148, doi:10.1109/Access.2019.2930650 (2019).

515    18    Qi, L. *et al.* Cross-sectional photoacoustic tomography image reconstruction with a multi-
516        curve integration model. *Computer Methods and Programs in Biomedicine* **197**,
517        doi:10.1016/j.cmpb.2020.105731 (2020).

518    19    Zhang, S. *et al.* Photoacoustic imaging of living mice enhanced with a low-cost contrast
519        agent. *Biomed Opt Express* **10**, 5744-5754, doi:10.1364/BOE.10.005744 (2019).

520    20    Li, X. *et al.* Multispectral Interlaced Sparse Sampling Photoacoustic Tomography. *IEEE*
521        *Transactions on Medical Imaging*, 1-1, doi:10.1109/tmi.2020.2996240 (2020).

522    21    Keshava, N. & Mustard, J. F. Spectral unmixing. *IEEE Signal Processing Magazine* **19**,
523        44-57, doi:10.1109/79.974727 (2002).

524    22    Yousaf, T., Dervenoulas, G. & Politis, M. Advances in MRI Methodology. *Int Rev*
525        *Neurobiol* **141**, 31-76, doi:10.1016/bs.irn.2018.08.008 (2018).

526    23    Wang, L. V. & Hu, S. Photoacoustic tomography: in vivo imaging from organelles to
527        organs. *Science* **335**, 1458-1462, doi:10.1126/science.1216210 (2012).

528    24    Wang, L. V. & Yao, J. A practical guide to photoacoustic tomography in the life sciences.
529        *Nat Methods* **13**, 627-638, doi:10.1038/nmeth.3925 (2016).

530    25    Nie, L. & Chen, X. Structural and functional photoacoustic molecular tomography aided
531        by emerging contrast agents. *Chem Soc Rev* **43**, 7132-7170, doi:10.1039/c4cs00086b
532        (2014).

533    26    Sivasubramanian, K. & Pramanik, M. High frame rate photoacoustic imaging at 7000
534        frames per second using clinical ultrasound system. *Biomedical Optics Express* **7**,
535        doi:10.1364/boe.7.000312 (2016).

536    27    Glasser, M. F. *et al.* The Human Connectome Project's neuroimaging approach. *Nat*
537        *Neurosci* **19**, 1175-1187, doi:10.1038/nn.4361 (2016).

538    28    Ntziachristos, V. & Razansky, D. Molecular imaging by means of multispectral
539        optoacoustic tomography (MSOT). *Chem Rev* **110**, 2783-2794, doi:10.1021/cr9002566
540        (2010).

541    29    Ren, W. *et al.* Automated registration of magnetic resonance imaging and optoacoustic
542        tomography data for experimental studies. *Neurophotonics* **6**, 025001,
543        doi:10.1117/1.NPh.6.2.025001 (2019).

544    30    Ni, R., Vaas, M., Ren, W. & Klohs, J. Noninvasive detection of acute cerebral hypoxia
545        and subsequent matrix-metalloproteinase activity in a mouse model of cerebral ischemia
546        using multispectral-optoacoustic-tomography. *Neurophotonics* **5**, 015005,
547        doi:10.1117/1.NPh.5.1.015005 (2018).

548    31    Ju, Y. *et al.* Monodisperse Au-Fe2C Janus Nanoparticles: An Attractive Multifunctional
549        Material for Triple-Modal Imaging-Guided Tumor Photothermal Therapy. *ACS Nano* **11**,
550        9239-9248, doi:10.1021/acsnano.7b04461 (2017).

551    32    Ke, K. *et al.* Copper Manganese Sulfide Nanoplates: A New Two-Dimensional
552        Theranostic Nanoplatform for MRI/MSOT Dual-Modal Imaging-Guided Photothermal
553        Therapy in the Second Near-Infrared Window. *Theranostics* **7**, 4763-4776,
554        doi:10.7150/thno.21694 (2017).

555    33    Hupple, C. W. *et al.* A light-fluence-independent method for the quantitative analysis of
556        dynamic contrast-enhanced multispectral optoacoustic tomography (DCE MSOT).
557        *Photoacoustics* **10**, 54-64, doi:10.1016/j.pacs.2018.04.003 (2018).

558    34    Gehrung, M., Tomaszewski, M., McIntyre, D., Disselhorst, J. & Bohndiek, S. Co-
559        registration of optoacoustic tomography and magnetic resonance imaging data from

560    murine tumour models. *Photoacoustics* **18**, 100147, doi:10.1016/j.pacs.2019.100147
561    (2020).
562  35  Ren, W., Dean-Ben, X. L., Augath, M. A. & Razansky, D. Development of concurrent
563    magnetic resonance imaging and volumetric optoacoustic tomography: A phantom
564    feasibility study. *J Biophotonics* **14**, e202000293, doi:10.1002/jbio.202000293 (2021).
565  36  Sakka, S. G. & van Hout, N. Relation between indocyanine green (ICG) plasma
566    disappearance rate and ICG blood clearance in critically ill patients. *Intensive Care Med*
567    **32**, 766-769, doi:10.1007/s00134-006-0109-6 (2006).
568  37  Liu, Y. *et al.* Highly specific noninvasive photoacoustic and positron emission
569    tomography of brain plaque with functionalized croconium dye labeled by a radiotracer.
570    *Chem Sci* **8**, 2710-2716, doi:10.1039/c6sc04798j (2017).
571  38  Zhang, D. *et al.* Cell membrane coated smart two-dimensional supraparticle for in vivo
572    homotypic cancer targeting and enhanced combinational theranostics. *Nanotheranostics* **5**,
573    275-287, doi:10.7150/ntno.57657 (2021).
574  39  Yao, L., Sun, Y. & Jiang, H. Quantitative photoacoustic tomography based on the
575    radiative transfer equation. *Opt Lett* **34**, 1765-1767, doi:10.1364/ol.34.001765 (2009).
576  40  Brochu, F. M. *et al.* Towards Quantitative Evaluation of Tissue Absorption Coefficients
577    Using Light Fluence Correction in Optoacoustic Tomography. *Ieee Transactions on*
578    *Medical Imaging* **36**, 322-331, doi:10.1109/Tmi.2016.2607199 (2017).
579  41  Li, J. *et al.* Spatial heterogeneity of oxygenation and haemodynamics in breast cancer
580    resolved in vivo by conical multispectral optoacoustic mesoscopy. *Light: Science &*
581    *Applications* **9**, doi:10.1038/s41377-020-0295-y (2020).
582  42  Martin, J. D., Fukumura, D., Duda, D. G., Boucher, Y. & Jain, R. K. Reengineering the
583    Tumor Microenvironment to Alleviate Hypoxia and Overcome Cancer Heterogeneity.
584    *Cold Spring Harb Perspect Med* **6**, doi:10.1101/cshperspect.a027094 (2016).
585  43  Albini, A., Tosetti, F., Li, V. W., Noonan, D. M. & Li, W. W. Cancer prevention by
586    targeting angiogenesis. *Nat Rev Clin Oncol* **9**, 498-509, doi:10.1038/nrclinonc.2012.120
587    (2012).
588  44  Alexandrakis, G., Rannou, F. R. & Chatziioannou, A. F. Tomographic bioluminescence
589    imaging by use of a combined optical-PET (OPET) system: a computer simulation
590    feasibility study. *Physics in Medicine and Biology* **50**, 4225-4241, doi:10.1088/0031-
591    9155/50/17/021 (2005).
592  45  Schweiger, M. & Arridge, S. The Toast++ software suite for forward and inverse
593    modeling in optical tomography. *J Biomed Opt* **19**, 040801,
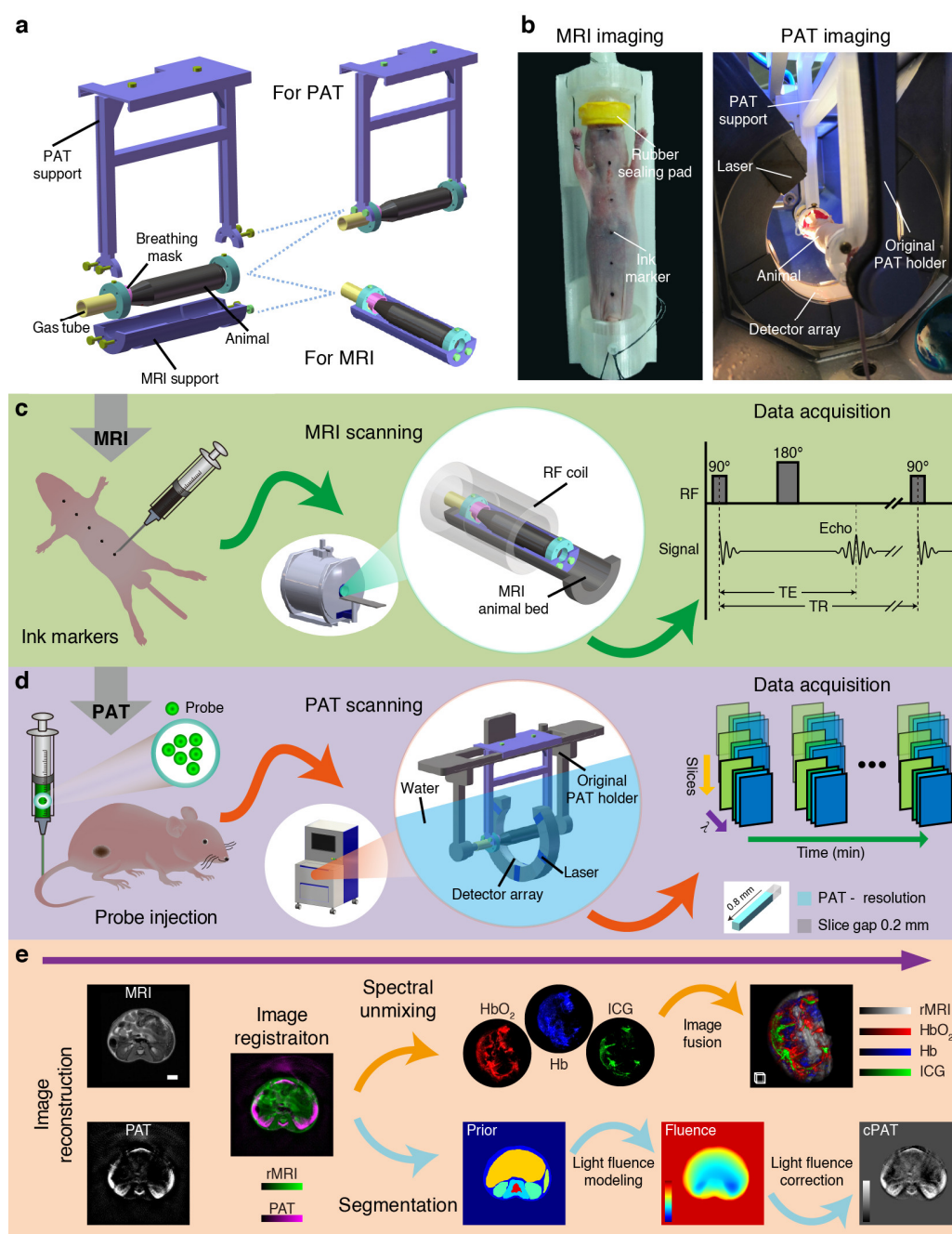594    doi:10.1117/1.JBO.19.4.040801 (2014).

## Acknowledgements

**Fig. 1 Co-registered hybrid-contrast imaging of living mice by successive PAT and MRI. a** The dual-modality imaging bed includes a PAT support, a MRI support, a gas tube, a breathing mask, two fixing plates and two ancillary supports. Image acquisition for the two modalities can be realized by assembling different components. **b** Photographs of a nude mouse placed on the animal bed before MRI and during PAT imaging. **c** MRI image acquisition process. Axial marker assignment: the skin surface of nude mice is marked with Chinese ink. MRI scanning: after assembling the MRI support, the animal was placed on the animal bed and transferred to the centre of the magnet for scanning. MRI data acquisition: a 2-D spin echo sequence was used to acquire MRI images. **d** PAT image acquisition process. Probe injection: optional exogenous probe such as ICG was injected through the tail vein. PAT scanning: after assembling the PAT support, the animal was loaded into the PAT imaging chamber filled with water for scanning. PAT data acquisition: 5-D multi-wavelength multi-slice longitudinal PAT images are acquired. **e** Image post-processing process. This process includes image reconstruction, image registration, spectral unmixing, image fusion, and PAT light fluence correction. See text and Supplementary Methods for more detail on image post-processing. Scale bars, 3 mm. Scale box, 1 mm$^3$. Details of the dual-modality imaging bed are shown in Supplementary Video 1 and Supplementary figure 1 and 2.
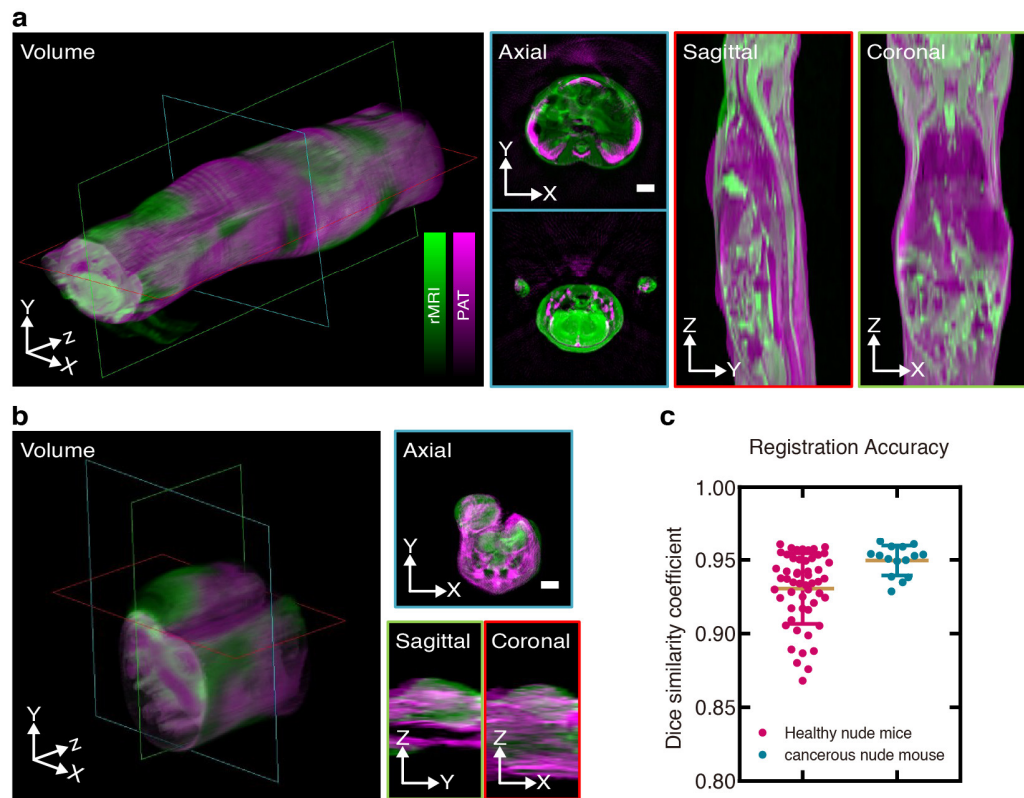
23

**Fig. 2 Spatial co-registration results. a** The registered PAT-MRI dual-modality images from healthy nude mouse. **b** The registered PAT-MRI dual-modality images from tumorous nude mouse. All images in (**a**) and (**b**) are displayed with pseudo-color overlay (magenta for PAT and green for MRI). All sagittal and coronal images are resampled and interpolated from the XY plane image stack, and display in 3D as volume images. **c** Quantification of the co-registration accuracy in Dice similarity coefficient using image data from (**a**) and (**b**). Scale bars, 3 mm.
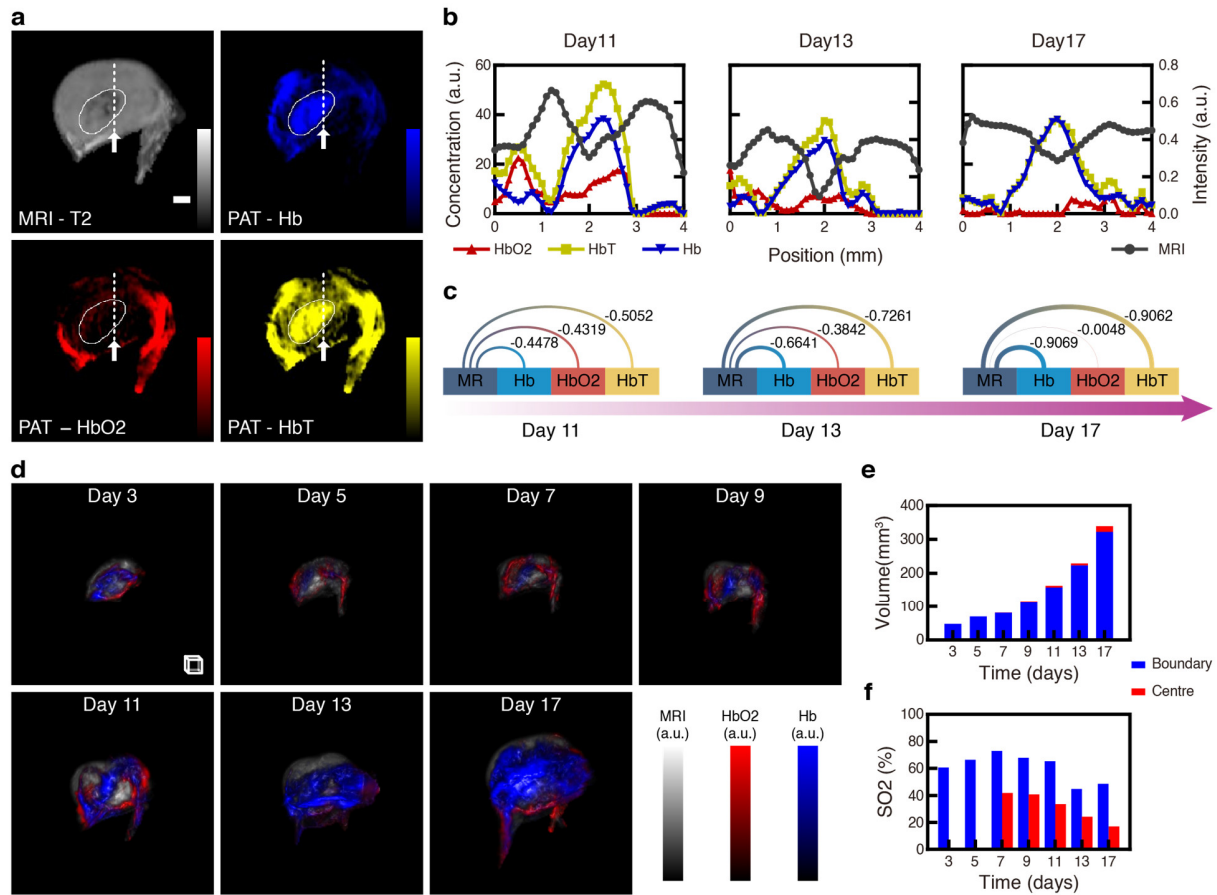
**Fig. 3 Week-long longitudinal monitoring of tumor dimension and hypoxia microenvironment in living nude mouse by PAT-MRI imaging. a** MRI image and PAT-derived Hb, $HbO_2$ and HbT images in the central XY plane of the 4T1 tumor. The white solid-line area depicts the regions with similar or opposite features. **b** Image profiles drawn along the straight white dashed-lines in (**a**). **c** Pearson correlation coefficients of the profiles between the Hb, $HbO_2$, HbT images and the MRI image. **d** 3D fusion display of MRI images and Hb, $HbO_2$ images in longitudinal imaging of the 4T1 tumor. We delineated the mask of hypoxic regions inside the tumor and computed the volume size (**e**) from MRI images and the blood oxygen saturation (**f**) from PAT images in the centre and boundary of the tumor separately. Scale bar, 1 mm. Scale box, 1 $mm^3$. See also Supplementary Fig. 6 and Supplementary Video 2.
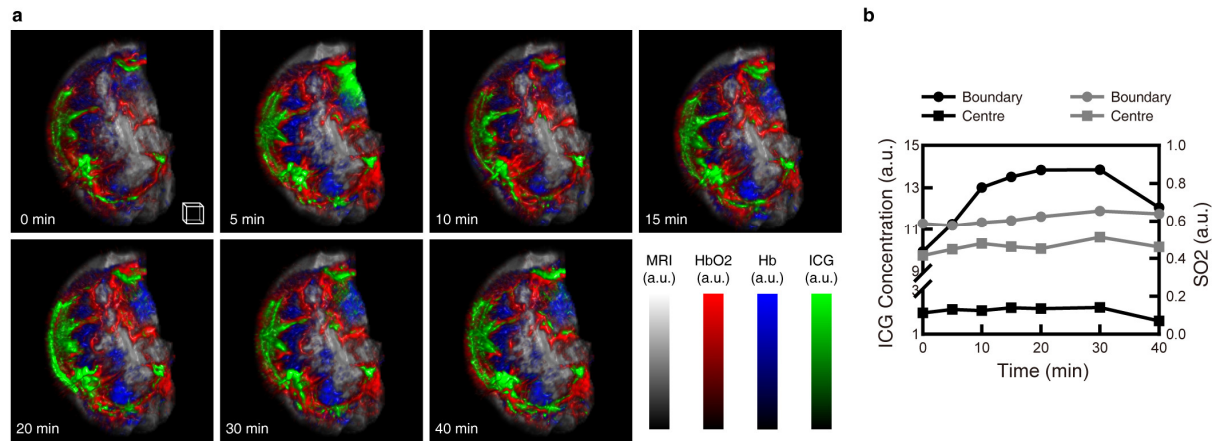
**Fig. 4 Temporal anatomical-molecular imaging of ICG perfusion inside 4T1 tumor. a** 3D fusion display of the Hb, HbO$_2$, ICG distributions on top of a co-registered MRI image of the 4T1 tumor microenvironment. PAT images were acquired at a 5 minute interval. **b** Time trace of the ICG concentration and SO$_2$ of the hypoxic centre and boundary region of the tumor. Scale box, 1 mm$^3$. See Supplementary Video 3.
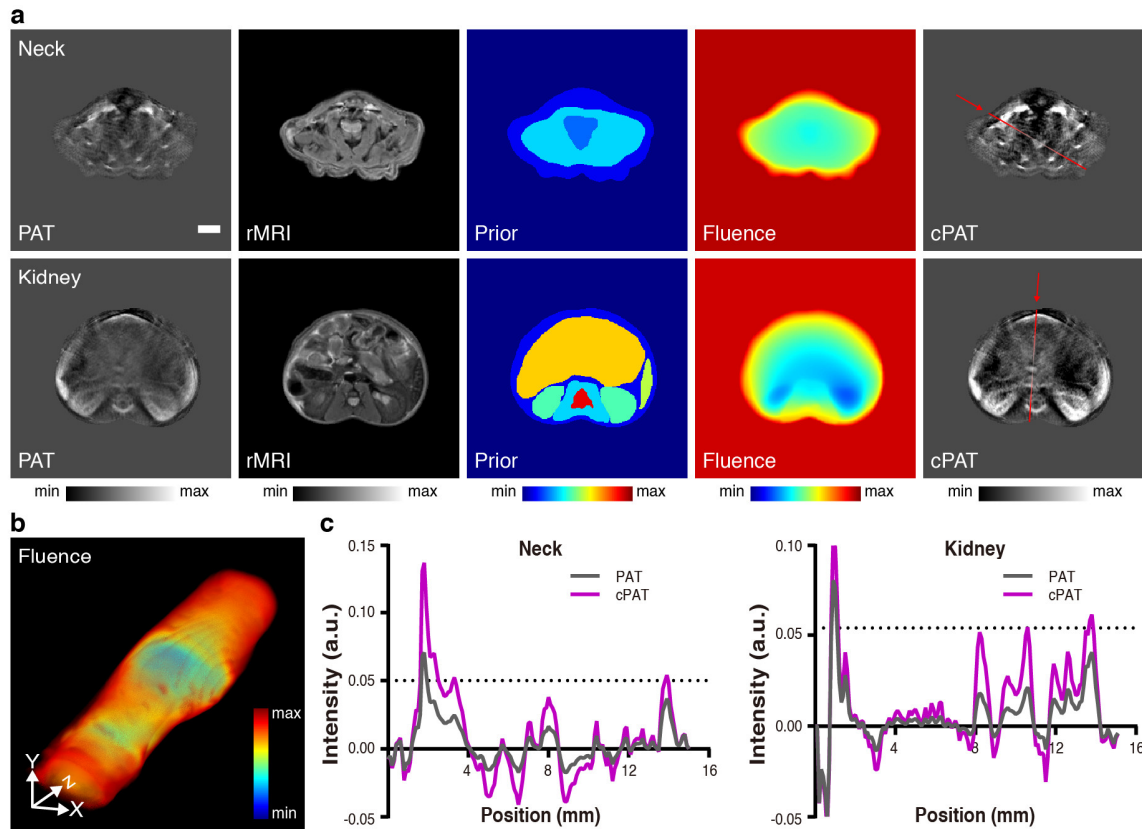
**Fig. 5 MRI structural guided light fluence correction for nude mouse PAT imaging *in vivo*. a** Light fluence correction results at the neck and the kidney position. PAT: raw PAT images. rMRI: co-registered MRI images. Prior: organ-level MRI segmentation results used to guide light fluence estimation. Fluence: light fluence distribution solved by the proposed optimization algorithm based on the Prior image. cPAT: light fluence corrected PAT images. **b** 3D view of light fluence distribution obtained with structural guidance from MRI. **c** Image profiles drawn along the straight red solid lines in (**a**). PAT imaging wavelength: 700 nm. Scale bar, 3 mm. The 3D segmentation results of MRI images and the obtained 3D light fluence distribution are shown in Supplementary Video 4.